J. Fluid Mech. (1997), *vol.* 339, *pp.* 173–198. Printed in the United Kingdom

A laboratory study of baroclinic waves and turbulence in an internally heated rotating fluid annulus with sloping endwalls

By MARK E. BASTIN AND PETER L. READ

Department of Physics, Sub-Department of Atmospheric, Oceanic and Planetary Physics, Clarendon Laboratory, Parks Road, Oxford, OX1 3PU, UK

(Received 2 February 1996 and in revised form 30 December 1996)

New laboratory experiments have been performed in a rotating fluid annulus, subject to internal heating and sidewall cooling, in which a radial depth gradient has been created by the inclusion of oppositely sloping boundaries. Endwall configurations that cause the fluid depth (D) to increase with radius ($\partial D/\partial r > 0$) and to decrease with radius ($\partial D/\partial r < 0$) have been studied, as the former is applicable to the terrestrial atmosphere and oceans, while the latter may be relevant to deep atmospheres such as those of the giant planets.

Even with the steepest boundary slopes, isolated or periodic chains of stable coherent eddies are observed with both endwall configurations, and these regular eddy modes are seen to drift relative to the walls of the convection chamber concordant with simple Rossby wave ideas. When the boundary slope (δ) is small, no difference is observed in the range of azimuthal wavenumbers seen in the regular wave regimes of the two endwall configurations. At larger values of δ, however, this symmetry is lost, since regular modes $m = 2$ to 8 are observed with $\partial D/\partial r > 0$ endwalls, while only a large vertically trapped anticyclonic gyre is seen with $\partial D/\partial r < 0$ endwalls. The other effects of the radial depth gradient are the observed reduction in both the lateral and vertical scale of the eddy features, and the formation of two independent trains of eddies within the gap width at sufficiently high rotation rates in the $\partial D/\partial r > 0$ endwall experiments. The zonal mean flow is also found to develop a significant barotropic component, superimposed on the vertically and horizontally sheared zonal jets generated by the non-monotonic thermal gradient of the experiment. This barotropic component is predominantly prograde (retrograde) in the $\partial D/\partial r > 0$ ($\partial D/\partial r < 0$) endwall experiments, and confined close to the outer (inner) wall where the fluid depth is greatest.

There is evidence of the formation of increased numbers of zonal jets in the $\partial D/\partial r > 0$ endwall experiments above that expected from the form of the thermal forcing. These multiple zonal jets are highly localized in the vertical, and are trapped close to the top boundary. Their radial scale is, nevertheless, close to that given by the Rhines argument. No comparable increase in the radial wavenumber of the mean flow is observed in the $\partial D/\partial r < 0$ endwall experiments in the present system.

1. Introduction

In this paper we report new experiments on free thermal convection in an internally heated rotating fluid annulus (Hide & Mason 1970; Quon 1977; Ukaji 1979; Read

1986*b*; Tamaki & Ukaji 1986; Read, Lewis & Hide 1997 (hereafter referred to as RLH)), where a radial depth gradient has been created by the inclusion of oppositely sloping endwalls. In a barotropic fluid, this endwall arrangement can be shown (Veronis 1963) to be completely equivalent to the β-effect (the variation in Coriolis parameter with latitude), and hence introduce a dispersive component to the flow. This direct equivalence is lost in a baroclinic fluid, since introducing β into the quasi-geostrophic potential vorticity equation, for example, directly alters the eigenfunctions, while sloping endwalls enter only into the boundary conditions. Nevertheless, oppositely sloping lids and bases are the simplest endwall configuration that can be used in the laboratory to simulate the azimuthal wave propagation and dispersive effects produced by β. However, other important properties such as the meridional and vertical wave propagation characteristics cannot be reproduced with these boundary conditions. Sloping boundaries that cause the fluid depth to increase with radius ($\partial D/\partial r > 0$) and to decrease with radius ($\partial D/\partial r < 0$) have both been studied. The former arrangement is applicable to a shallow layer of fluid on a sphere, for example the terrestrial atmosphere and oceans, where the depth of fluid columns parallel to the planetary axis of rotation increases with decreasing latitude. Conversely, the second endwall configuration may be relevant to the deep fluid envelopes of the giant planets, where the lack of a large solid lower boundary causes the depth of fluid columns parallel to the rotation axis to decrease with increasing distance from the latter (Busse 1976; Ingersoll & Pollard 1982; Ingersoll & Miller 1986).

Hide & Mason (1970) have shown from simple thermal arguments that if heat is removed equally from both sidewalls in an internally heated, rotating fluid annulus with horizontal endwalls (f-plane), the flow near the top surface will consist of closed re-circulating anticyclonic eddies. These stable eddy features are centred close to mid-radius and in the shear zone which exists between the two opposing zonal jets created by the horizontal non-monotonic thermal gradient of the experiment. The geophysical motivation for the study of these internally heated and sidewall-cooled flows comes from the suggestion (Read & Hide 1983, 1984; Read 1986*a*; Hide, Lewis & Read 1994) that there may be a dynamical similarity between the predominantly baroclinic eddies of this experiment and the major long-lived oval eddies seen in the atmospheres of Jupiter, Saturn and Neptune. The linear perturbation theory of Hide (1969) suggests, however, that the introduction of steep oppositely sloping endwalls should radically alter the structure of the laboratory eddies by causing each individual wave component to propagate with a phase speed which is dependent on its radial and azimuthal wavenumber. If stable eddies are seen with oppositely sloping boundaries, then a detailed comparison of their horizontal and vertical structure with that of the internally heated f-plane flows described by RLH will not only illustrate how the presence of a radial depth gradient modifies the flow structure in this experiment, but may also provide further clues to understanding the dynamics and stability of atmospheric flows.

Previous experimental studies on the effect of oppositely sloping endwalls on baroclinic instability have concentrated on the wall-heated rotating fluid annulus (Mason 1975), where the lateral temperature gradient is provided by the differential heating of the sidewalls. At low rotation rates Mason observed stable regular wave modes with azimuthal wavenumbers between $m = 1$ and 6, with m being dependent on the endwall slope and the sign of the impressed lateral temperature gradient. As the rotation rate was increased, however, he observed that the radial scale of the waves decreased to less than that of the gap width, so that ultimately two separate wave trains formed at the inner and outer cylinders. In the present set of experiments,

we will investigate whether the radial scale of the internally heated and sidewall cooled flows is affected in a similar manner, and if there is any quantitative difference between the radial confinement produced by the two opposite senses of endwall slope.

The horizontal non-monotonic thermal gradient produced by internal heating and sidewall cooling in these experiments is expected to generate two opposing zonal jets at each horizontal measurement level in the fluid. In the corresponding f-plane experiments of RLH, these opposing zonal jets are seen to be centred close to the top and bottom boundaries, and reverse sign about the level of no mean motion which approximately coincides with mid-depth. The introduction of a radial depth gradient might be expected to alter this basic background mean flow structure, perhaps by blocking the spectral evolution of the barotropic component of the flow (Rhines 1975, 1979). Briefly, Rhines argues that a geostrophically turbulent fluid which possesses a stable density stratification can convert potential energy from its vertically sheared baroclinic modes to kinetic energy in the form of depth-independent barotropic modes. The evolution of the latter may then be approximated to that of two-dimensional turbulence. In the presence of β, the inverse energy cascade of freely evolving two-dimensional turbulence (characterized by the total eddy wavenumber K, and the r.m.s. particle velocity U) is blocked when the average wave steepness, $2UK^2/\beta$, declines below unity, or when the growing eddies can radiate their accumulating energy through Rossby wave propagation. Since the turbulent cascade associates smaller wavenumbers with smaller frequencies and the Rossby wave regime associates smaller wavenumbers with larger frequencies, the Rhines scale $L_\beta = \pi(2U/\beta)^{1/2}$ may be expected to be the dominant scale within the flow. The anisotropy of the Rossby wave dispersion relationship allows a further limited transfer of energy to smaller frequencies if the lateral scale of the eddies shrinks while their zonal scale increases. If the initial energy spectrum is evenly distributed in spectral space, Rhines argues that the end state for this cascade is the formation of alternating easterly and westerly zonal jets of lateral scale L_β. It is clearly of interest to investigate whether the basic background zonal mean flow structure is altered by the inclusion of oppositely sloping endwalls, and whether there is evidence for the blocking of the inverse energy cascade at the Rhines scale in the present system with its complicated thermal structure.

The outline of this paper is therefore as follows. A brief description of the experimental configuration is given in §2, while §3 explains how the velocity data obtained from the system has been analysed to produce the various diagnostics used in this study. Section 4 discusses the results obtained from the experiment, and is split into two parts. The first, §§4.1–4.3, investigates whether stable eddy structures are observed with oppositely sloping endwalls, and if there is any difference between the flows seen with the two senses of endwall slope. The horizontal and vertical structure of these flows are then described in detail and compared with those seen in the f-plane experiments of RLH in order to identify how the introduction of a radial depth gradient modifies the flow regimes. The angular phase velocities of the stable eddy modes observed in these experiments are then calculated and compared with those of barotropic Rossby waves. The second part of this section, §§4.4–4.6, investigates how the zonal mean flow profiles are altered by the different endwall arrangements, and examines whether the observed increase in the radial wavenumber of the zonal mean flow can be linked to the Rhines effect. Finally, §5 summarizes and discusses the main results of this study and suggests further experiments which could extend this work.

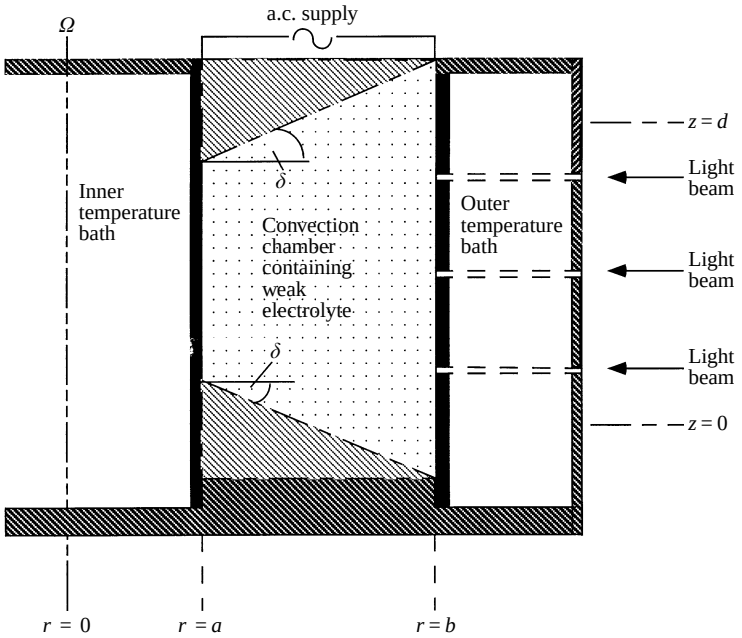

FIGURE 1. Schematic cross-section of the cylindrical annulus used in the experiments with endwalls that cause the fluid depth to increase with radius ($\partial D/\partial r > 0$).

2. Experimental details

The experiment consisted of two vertical co-axial thermally conducting copper-coated brass cylinders of radii 41 and 102 mm respectively shown in figure 1. The cylinders were mounted on a solid non-conducting horizontal base so that there was a uniform annular gap of 61 mm between them. This annular region was filled with a water/glycerol working solution of a sufficient density to allow the fluid to be seeded with neutrally buoyant polystyrene beads (600 μm diameter), which acted as tracers for flow visualization and velocity measurement. The convection chamber was centred on a level turntable, and was rotated by a servo-controlled permanent-magnet d.c. motor, giving rotation rates between 0.01 and 4.5 rad s^{-1}.

The thermal forcing in these experiments was provided by the passing of an a.c. electric current through the body of the fluid (cf. Hide & Mason 1970), to which trace amounts of an inorganic copper salt ($CuCl_2$) had been added. This caused the fluid to act as an electrolyte, with the inner and outer cylinders being the electrodes. Adjacent to both cylinders were water baths through which water at a carefully controlled temperature (typically $\pm$ 0.02 K) was passed. By maintaining both sidewalls at the same temperature ($\sim$ 20 °C), the heat generated in the convection chamber was removed simultaneously at both sidewalls. The impressed temperature contrast in the convection chamber was then determined by the power input, which was calculated from measurements of the r.m.s. voltage (up to 300 V) and current applied to the sidewalls, the physical geometry of the system, and the thermal properties of the working fluid. All runs were performed by maintaining a constant power input (approximately 100 W) and spinning up the apparatus from rest to the required rotation rate Ω for each run. The rotation rate was systematically increased in steps of 0.05 rad s^{-1} which is the effective 'resolution' of these experiments.

Flow visualization was achieved by making the outer cylinder (and its water

Radius of inner and outer cylinders	a,b	41, 102 mm
Angular velocity	Ω	0–4.5 rad s^{-1}
Power input	$\bar{P}_0$	95–105 W
Coef. cubic expansion	α	3.10–3.16 $\times 10^{-4}$ K^{-1}
Kinematic viscosity of fluid	ν	1.30–1.52 $\times 10^{-2}$ cm^2 s^{-1}
Thermal diffusivity	κ	1.30–1.32 $\times 10^{-3}$ cm^2 s^{-1}
Specific heat capacity of fluid	C_p	3.84–3.85 J g^{-1} K^{-1}
Mean density of fluid	$\bar{\rho}$	1.047–1.049 g cm^{-3}
Depth of fluid at mid-radius	$\overline{D}$	13.8 (35°), 15.8 (12°) cm
Height of measurement levels	$z/\overline{D}$	0.72, 0.44, 0.16 (35°)

TABLE 1. General experimental dimensions, and working fluid parameters.

bath) in four separate sections, with a 5 mm transparent acrylic insert between each part. Horizontal flow velocity fields were obtained using the particle tracking system described by Hignett *et al*. (1985). Under computer control the convection chamber was illuminated cyclically at one of three measurement levels in the vertical with flat horizontal sheets of light. The light scattered from the polystyrene beads was collected by a monochrome closed-circuit TV camera mounted approximately 1.5 m above the geometric centre of the convection chamber. Each image was then digitized and sent to a PDP 11/34 minicomputer where the motions of individual particles between frames allowed the determination of their trajectories over a time interval of approximately 3.6 s. A scan of each measurement level typically produced a horizontal velocity field with 200–500 randomly distributed velocity vectors.

The fluid was in contact with rigid non-conducting radially sloping top and bottom boundaries, whose slopes were either 12° or 35° to the horizontal. The lids were made of clear Perspex so the light scattered from tracer particles in the flow could be seen by the camera mounted directly overhead. The top surfaces of these lids were also shaped to provide additional optical correction. The lids and bases sloped so that there was either an increase in fluid depth with radius ($\partial D/\partial r > 0$), or there was a decrease in fluid depth with radius ($\partial D/\partial r < 0$). Four different endwall configurations were investigated (with the magnitude of the endwall slope being the same for the top and bottom boundaries), namely 12° $\partial D/\partial r > 0$, 12° $\partial D/\partial r < 0$, 35° $\partial D/\partial r > 0$ and 35° $\partial D/\partial r < 0$. In the rest of the paper these different experimental sets will be referred to as the +12°, −12°, +35° and −35° experiments. A barotropic β-term for each run in these experiments may be obtained from consideration of the potential vorticity equation for an incompressible inviscid two-dimensional fluid layer, and has the form

$$\beta = \pm \frac{4\Omega \tan(\delta)}{\overline{D}}, \tag{2.1}$$

where $\overline{D}$ is the mean fluid depth at mid-radius. Values of $\overline{D}$ for each experimental configuration are given in table 1.

3. Velocity data analysis

The 'raw' velocity data of the experiment were reconstructed on an evenly spaced annular grid by fitting a truncated set of orthogonal basis functions (by the method of least-squares) to the radial and azimuthal velocity components. The fitted function consisted of the product of a discrete set of sixteen Fourier modes in the azimuthal

direction ($m = 0, 15$), and a series of six 'cylindrical sine' functions in the radial direction ($l = 1, 6$). It has the form

$$(u, v) = \left(\frac{b}{r}\right)^{1/2} \left(\sum_{m=0}^{15} \sum_{l=1}^{6} a_{m,l}^{(u,v)} \sin(l\pi x) \cos(m\theta) + b_{m,l}^{(u,v)} \sin(l\pi x) \sin(m\theta) \right), \quad (3.1)$$

where θ is the azimuthal angle, and x is the scaled radius, $x = (r - a)/(b - a)$. The regression coefficients $a_{m,l}$, $b_{m,l}$ were calculated for both the radial (u) and azimuthal (v) velocity components by minimizing the square of the difference of the above function from the raw velocity data (Jackson & Hignett 1984; Bell 1984; Bell & Jackson 1985). The $m = 0$ azimuthal mode represents the zonal mean flow, while the fifteen remaining azimuthal wavenumbers represent the 'eddy' components.

3.1. *Eddy spectral energy density*

A one-dimensional spectral energy density plot of the radial (shown here) and azimuthal eddy kinetic energy against total dimensional wavenumber

$$\kappa = \left[\left(\frac{2m}{b + a} \right)^2 + \left(\frac{\pi l}{b - a} \right)^2 \right]^{1/2}, \quad (3.2)$$

can be obtained directly from the 90 (15 by 6) individual eddy kinetic energy components

$$\frac{1}{2} \frac{\int_a^b | u(m, l) |^2 \, r \mathrm{d}r}{\int_a^b r \mathrm{d}r} = \frac{b}{4(b + a)} \sum_{m=0}^{15} \sum_{l=1}^{6} \left(a_{m,l}^2 + b_{m,l}^2 \right), \quad (3.3)$$

derived from the least-squares-fitted regression coefficients of equation (3.1). The eddy spectral energy $E(\kappa)\,\mathrm{d}\kappa$ is then calculated by summing those eddy kinetic energy components which fall within a small interval in κ, $\mathrm{d}\kappa$ (0.5 cm^{-1}), which is moved in steps (0.1 cm^{-1}) from $\kappa_{min} = 0.534$ cm^{-1} (m, l = 1, 1) to $\kappa_{max} = 3.735$ cm^{-1} (m, l = 15, 6). The spectral energy density $E(\kappa)$ is then obtained by dividing by the width of the interval $\mathrm{d}\kappa$, and is then averaged over a number of scans to produce time-averaged spectra. Although the range in total wavenumber space is probably not sufficient to resolve fully the inertial ranges suggested by the statistical theories of geostrophic turbulence (Charney 1971), enough modes are fitted to the data to allow the determination of the scales of maximum eddy kinetic energy. Comparison of this scale with the Rhines scale may then provide insight into whether the inverse energy cascade of the barotropic components of the flow is blocked at L_β.

3.2. *Velocity streamfunctions*

Horizontal streamfunction and velocity potentials can be determined from the Fourier components fitted to the raw velocity data of the experiment following the method of Read (1990). Furthermore, since most flows encountered in thermally forced rotating fluid experiments are in approximate quasi-geostrophic (QG) balance (Hide & Mason 1975), the streamfunction is roughly equivalent to the horizontal pressure field, thereby enabling QG potential vorticity fields to be derived from it.

The method works by representing the two-dimensional velocity fields as a linear superposition of a non-divergent rotational velocity component V_ψ and an irrotational divergent component V_χ (Batchelor 1967). Scalar streamfunction (ψ) and velocity

potential fields (χ) may be defined for V_ψ and V_χ, so that $V_\psi = \boldsymbol{k} \times \nabla\psi$ and $V_\chi = \nabla\chi$, where $\boldsymbol{k}$ is the unit vector perpendicular to the annular plane. Consideration of the form of the azimuthal (u) and radial (v) basis functions (3.1) fitted to the velocity data requires that two Poisson equations must be solved simultaneously to find ψ and χ. In cylindrical polar coordinates (with the application of the non-slip boundary conditions $\psi = 0$ at one sidewall, $\partial\psi/\partial r = 0$ at the other, and $\partial\chi/\partial r = 0$ at both sidewalls), the two Poisson equations are

$$\nabla_h^2\psi = \frac{1}{r}\frac{\partial(rv)}{\partial r} - \frac{1}{r}\frac{\partial u}{\partial\theta}, \tag{3.4}$$

and

$$\nabla_h^2\chi = \frac{1}{r}\frac{\partial(ru)}{\partial r} + \frac{1}{r}\frac{\partial v}{\partial\theta}. \tag{3.5}$$

Solutions for ψ and χ are obtained from the horizontal vorticity ($\nabla_h^2\psi$) and the divergence ($\nabla_h^2\chi$) fields in the form of four ordinary differential equations (for each azimuthal wavenumber), which can be solved by the 'shooting method'.

In the interior of rotating flows where the Rossby and Ekman numbers tend to be small, the approximate conservation of the QG potential vorticity Π places a powerful constraint on the time evolution of the flow, and can therefore be used as a flow tracer. To derive Π a uniform mean N^2 profile in the vertical is assumed (derived from temperature measurements at the top and bottom boundaries), and data are collected from three sequential measurement levels which are scanned as close together in time as possible. The presence of strong gradients in the flow, however, tends to produce errors of up to 20% in the amplitude of the field (Read 1990).

4. Experimental results

4.1. *Overview of flow regimes*

The main flow regimes exhibited in these oppositely sloping endwall experiments are broadly similar to those found in the internally heated f-plane studies (Hide & Mason 1970; RLH), depending strongly on the impressed temperature contrast and the rotation rate Ω. As Ω is systematically increased there is a transition from purely axisymmetric flow, through a regular wave regime consisting of a numbers of stable eddy features, to fully irregular and disordered flow, which may be close to a state of 'geostrophic turbulence' (Hide & Mason 1975; Buzyna, Pfeffer & Kung 1984). These distinct flows may be ordered with respect to values of the dimensionless parameters: the Burger (S) and Taylor (τ) numbers. Specifically the Burger number is defined as the squared ratio of the Rossby deformation radius L_r to the annular gap width

$$S = \left(\frac{L_r}{b-a}\right)^2 = \frac{g\alpha\Delta T_z\overline{D}}{4\Omega^2(b-a)^2}, \tag{4.1}$$

where ΔT_z is a measure of the vertical temperature scale set up by the internal heating, and the other parameters are as indicated in table 1. The Taylor number is defined as

$$\tau = \frac{4\Omega^2(b-a)^5}{\nu^2\overline{D}}, \tag{4.2}$$

following Hide & Mason (1975). The vertical temperature scale and the other parameters were calculated from temperature measurements of the fluid, through a

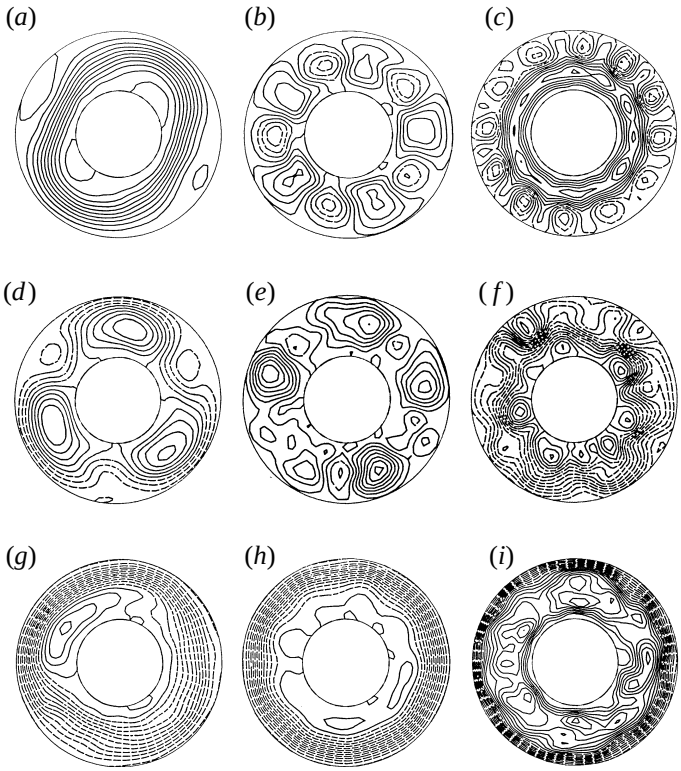

FIGURE 2. A representative sample of the range of flows at the upper measurement level ($z/\overline{D} = 0.72$) obtained with $+35°$ (a–c), f-plane (d–f) and $-35°$ (g–i) endwall configurations. Fields shown are total horizontal streamfunction maps corresponding to the following conditions: (a) $m = 2$ ($S = 0.902$, $\tau = 1.48 \times 10^6$); (b) $m = 5$ ($S = 0.152$, $\tau = 1.11 \times 10^7$); (c) double eddy train ($S = 0.013$, $\tau = 1.96 \times 10^8$); (d) $m = 3$ ($S = 0.400$, $\tau = 3.41 \times 10^6$); (e) $m = 4/5$ wavenumber vacillation ($S = 0.014$, $\tau = 2.68 \times 10^7$); (f) irregular ($S = 3.61 \times 10^{-3}$, $\tau = 7.58 \times 10^7$); (g) $m = 1$ ($S = 0.233$, $\tau = 6.40 \times 10^6$); (h) irregular ($S = 0.091$, $\tau = 1.76 \times 10^7$); (i) irregular ($S = 0.015$, $\tau = 1.97 \times 10^8$). Contour intervals are 2 (c, f, i) and 5 mm^2 s^{-1}.

series of 15 copper–constantan thermocouples placed flush with the surfaces of the inner and outer cylinders, and the top and bottom boundaries.

Figure 2 shows a set of total horizontal streamfunction maps, obtained at the upper level of the experiment ($z/\overline{D} = 0.72$), which represent the range of flows obtained with $+35°$ (a–c), f-plane (d–f) and $-35°$ (g–i) endwall configurations. These streamfunction maps represent regular (a, b, d, g), wavenumber vacillation (e), double eddy train (c) and irregular (f, h, i) flows. The regular wave regimes of the $+35°$ and $+12°$ experiments comprised single-wavenumber steady flows in the range $m = 2$ to 8 and $m = 3$ to 7. These regular eddy modes were observed to drift fairly quickly in an easterly, or clockwise, sense relative to the walls of the apparatus. Two examples of regular eddy flows seen in the $+35°$ experiment are shown in figure 2. The $m = 2$ mode (a), observed just inside the upper symmetric transition, consists of two small cyclones centred close to the inner cylinder and two anticyclones compressed near to the outer cylinder. As Ω is increased the wavenumber and structure of the regular eddy features change so that for the $m = 5$ mode (b) the anticyclonic eddies are now seen to fill the annular gap, while the cyclonic eddies have a slightly smaller radial scale, and are centred about mid-radius. Further increases in the Taylor

number caused the flow to become more disordered, with the eddies reducing their radial scale and becoming progressively more radially confined so that they no longer filled the gap width. At sufficiently high Taylor numbers, $\tau > 6.5 \times 10^7$ ($+35°$) and $\tau > 1.0 \times 10^8$ ($+12°$), the radial confinement became so strong that two independent trains of eddies, with apparently different phase speeds, were seen to form in the annular gap. This double eddy train was most evident at the upper measurement level of the experiment (*c*). The eddy train close to the outer cylinder was observed to consist mainly of cyclonic eddies, while that at the inner cylinder was dominated by anticyclones, this arrangement being consistent with the shear of the background flow at the different radii.

The range of regular modes found in the $-12°$ experiment was similar to that seen with $+12°$, that is $m = 3$ to $m = 7$. However, the regular regime of the $-35°$ set was found to consist solely of a single isolated anticyclonic eddy, which was only clearly visible at the upper level (*g*). It was found to drift very rapidly in a westerly sense relative to the apparatus, and was only observed over a small range in Taylor number $2.77 \times 10^6 \leqslant \tau \leqslant 1.23 \times 10^7$ ($0.62 \geqslant S \geqslant 0.12$). Moving to larger values of Taylor number, this gyre was seen immediately to break up directly into disordered flow at $\tau \geqslant 1.35 \times 10^7$ ($S < 0.12$), with no evidence for the existence of stable higher-wavenumber regular states (*h*). Further increases in Ω produced only more disorder in the flow, with the scale of the eddy features becoming progressively smaller (*i*).

Comparison of these oppositely sloping boundary flows with those of the *f*-plane experiment (*d–f*) not only illustrates the difference in the horizontal structure of the eddies in the different regular wave regimes, but also the effective reduction in the radial scale of the eddies produced in the $\partial D/\partial r > 0$ endwall experiments at high Taylor numbers (*c*). In the latter there is clear evidence for the organization of the flow, with radial confinement of the eddy features to different 'latitudinal bands', which is not seen in the *f*-plane example (*f*). This organization of the flow may be attributable to vortex partitioning, in which the various eddy components migrate to the radii corresponding to their respective absolute vorticity (Kuo 1950, 1951, 1953).

Figure 3 shows a schematic regime diagram of the non-axisymmetric flows seen in both the *f*-plane and oppositely sloping boundary experiments as a function of endwall slope and Taylor number. Each symbol represents a single run, and hence shows the effective 'resolution' in Taylor number space of the experiments. Apart from the $-35°$ set, the range in azimuthal wavenumber of regular modes is greater in the oppositely sloping boundary experiments than in the corresponding *f*-plane experiments, where only the regular modes $m = 3$ to 5 are observed. In the oppositely sloping boundary experiments there is the occasional example of two stable modes with different azimuthal wavenumber existing in the same region of parameter space. This overlap in dominant wavenumber is, however, smaller than that seen in the *f*-plane experiments, where the multiplicity of equilibrium states is found to increase with Taylor number (RLH). These hysteresis effects are, nevertheless, much less pronounced than in conventional wall-heated annulus flows, where no well-defined lower boundary in Θ (the stability parameter corresponding to S) is found to exist (see e.g. Hignett *et al*. 1985).

The axisymmetric flow regimes of the four oppositely sloping endwall configurations were observed to exist over the approximate range in Taylor number $\tau \leqslant 5.36 \times 10^5$ ($S \geqslant 2.44$) for $+35°$, $\tau \leqslant 1.79 \times 10^6$ ($S \geqslant 0.44$) for $+12°$, $\tau \leqslant 1.93 \times 10^6$ ($S \geqslant 0.64$) for $-12°$ and $\tau \leqslant 2.3 \times 10^6$ ($S \geqslant 0.73$) for $-35°$. The leftmost symbol for each endwall configuration in figure 3 suggests that there is a trend in the onset of

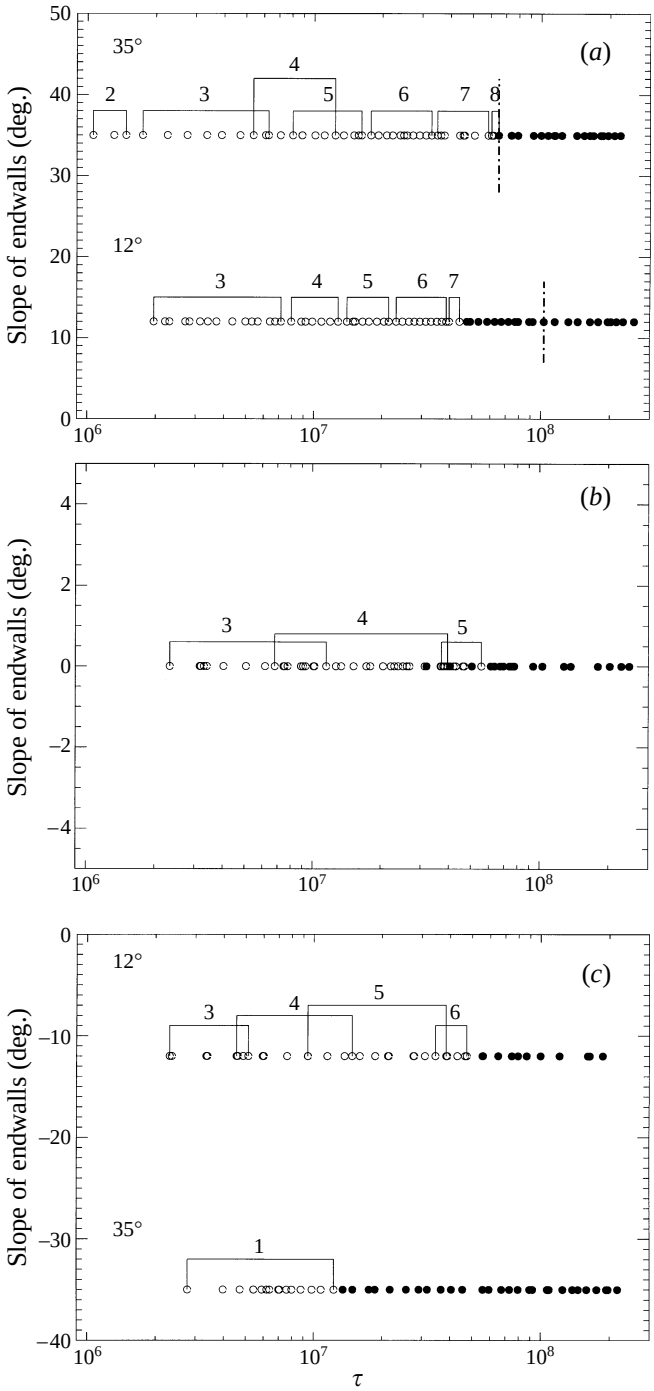

FIGURE 3. Schematic regime diagrams of the non-axisymmetric flows seen in the $\partial D/\partial r > 0$ (*a*), f-plane (*b*), and $\partial D/\partial r < 0$ (*c*) endwall experiments as a function of Taylor number. Regular (irregular) flow with the indicated azimuthal wavenumber m is denoted by open (closed) circles. The approximate onset of a double eddy train in the $+12°$ and $+35°$ experimental sets is indicated by the vertical dot-dashed lines.

instability in these experiments with $\partial D/\partial r < 0$ ($\partial D/\partial r > 0$) endwalls stabilizing (destabilizing) the wave regime. This is of interest since the linear perturbation theory of Hide (1969) cannot distinguish between these different endwall configurations, which both produce a stabilization of the wave regime (Mason 1975). The linear theory assumes isotherms with constant slope, which is clearly not the case with the complex non-monotonic thermal gradient of these experiments.

4.2. *Eddy horizontal and vertical structures*

As is clear from figures 2 and 3, isolated or periodic chains of eddies are a feature of all the oppositely sloping boundary configurations studied, even those with the steepest endwall slopes. The detailed structure of the eddies seen in the internally heated and sidewall cooled f-plane experiments have been extensively investigated in both numerical simulations (Read 1985) and laboratory measurements (RLH). Briefly, these internally heated f-plane eddies were found to have an equivalent-barotropic structure close to the 'thermal equator' (where $\partial T/\partial r \approx 0$), while being highly baroclinic on either side of it, with a phase slope that depended on the sign of $\partial T/\partial r$ in the azimuthally averaged mean flow. Apart from the weak waves confined towards the top boundary seen close to the upper symmetric transition, the radial and zonal amplitude of the fully developed waves in the f-plane experiment was found not to vary substantially with depth, being only slightly larger at the lower levels in the fluid. In the previous section it is apparent from the horizontal streamfunction maps that one of the principal effects of the radial depth gradient is to modify the lateral scale of the eddy features seen in the current experiment. Since such effects are not seen in the f-plane experiments, it is possible that the vertical structure of the regular modes seen in the present system may also depart from that found for the f-plane eddies, and this constitutes the subject we investigate in the present section.

Figures 4 and 5 show horizontal eddy streamfunction maps at the upper ($z/\overline{D} = 0.72$) and lower ($z/\overline{D} = 0.16$) levels in the experiment corresponding to the examples of $+35°$ and $-35°$ flow shown in figure 2. In the $+35°$ $m = 2$ mode (figure 4*a*, *d*), the eddy features have approximately equal strength at both levels, with the anticyclonic features tilting anticlockwise with height and the cyclones tilting clockwise with height (once the anticlockwise drift of the eddies between consecutive scans has been removed). As Ω is increased, however, the regular eddy features become stronger at the lower level, as is illustrated by the $m = 5$ mode (figure 4*b*, *e*). Further increases in Taylor number cause the radial scale of the eddy features to diminish so that ultimately two independent trains of eddies form in the gap width. The eddy field of such a flow is still surprisingly regular (figure 4*c*, *f*) with an alternating pattern of radially confined cyclones and anticyclones, which have approximately the same radial scale at both levels, whilst also being centred close to the outer cylinder. Once again the eddy features are slightly stronger at the lower level. This apparent vertical trapping of the eddies seen in the $+35°$ experiments towards the lower levels of the fluid is further illustrated in figure 6, which shows (r, z) cross-sections of the eddy radial velocity amplitude $\left(|\, u^2 \,|\right)^{1/2}$ for the regular $m = 5$ mode (*a*) and double eddy train flow (*b*) discussed above. In both cases the eddy radial velocity amplitude becomes larger as the bottom boundary is approached (although there is a maximum at mid-depth close to the inner cylinder in the double eddy train flow), while the radial confinement of the eddies close to the outer cylinder in the double eddy train flow (figure 4*c*, *f*) is also evident.

The boundary towards which the regular eddy modes become localized is reversed in the $\partial D/\partial r < 0$ experiments. This is illustrated in figure 5 where horizontal eddy

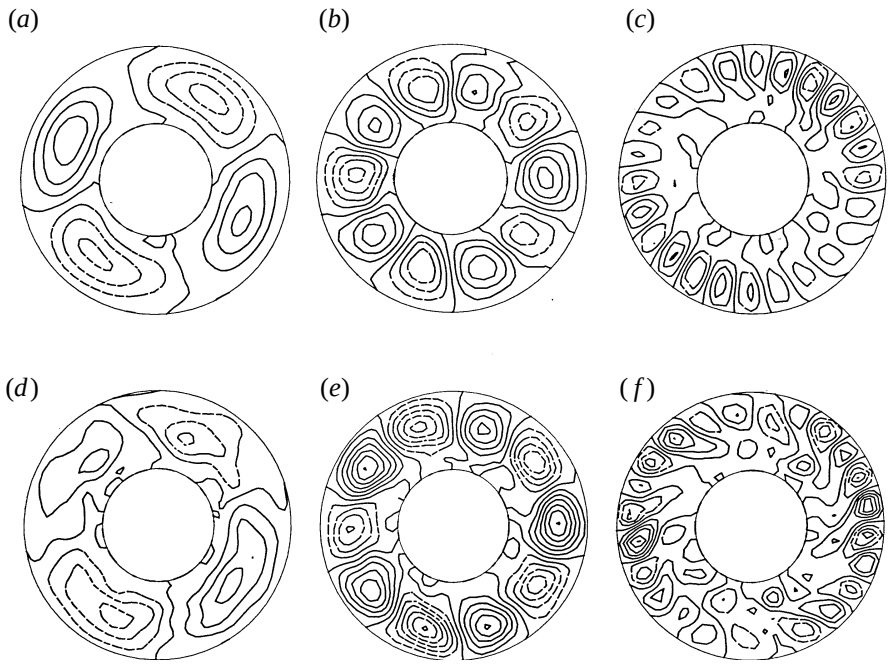

FIGURE 4. Eddy horizontal streamfunction maps at the upper ($z/\overline{D} = 0.72$) (a–c) and lower ($z/\overline{D} = 0.16$) (d–f) measurement levels for the $+35^\circ$ endwall configuration. Maps correspond to the $m = 2$, 5 and double eddy train flows shown in figure 2. The lower-level streamfunction maps for the two regular modes have been 'phase corrected' so that they are in the same time frame as the upper-level maps. Contour intervals are 2 (c, f) and 5 mm^2 s^{-1}.

streamfunction maps at upper and lower levels are shown for an example of a regular -35° $m = 1$ mode. The $m = 1$ mode is clearly much stronger at the upper measurement level. This anticyclonic eddy was, in fact, only visible at the upper level in the experiment, suggesting that it was vertically trapped quite close to the top boundary. The vertical trapping of this mode is further illustrated in figure 6(c), where the radial velocity amplitude of azimuthal wavenumber $m = 1$ is centred close to mid-radius and at the upper level. The other maxima seen close to the inner cylinder at the lower level may indicate the position of the accompanying cyclone visible in the eddy streamfunction maps (figure 5d). At the highest Taylor numbers, however, the eddy streamfunction plots show that the irregular eddies are now strongest at the lower level, and are centred close to the inner cylinder (figure 5f). This radial confinement is also evident in figure 6(d) where the dominant azimuthal wavenumber $m = 6$ is compressed close to the inner cylinder.

It is therefore evident that the variation in fluid depth with radius has a pronounced effect on both the horizontal and vertical structure of the eddies produced with internal heating and sidewall cooling. The reduction in the radial scale of the waves observed by Mason (1975) at high rotation rates and steep endwall slopes in his wall-heated experiments is also reproduced in the current study with the formation of the double eddy train at high Taylor numbers in the $\partial D/\partial r > 0$ endwall experiments. Although a reduction in the radial scale of eddies is also seen in the -35° experiments, it is less dramatic than in the $+35^\circ$ set, and a possible reason for this is outlined later. At the highest Ω the two senses of endwall slope are also seen to confine the eddies close to the outer cylinder with $\partial D/\partial r > 0$ endwalls, and close to the inner cylinder

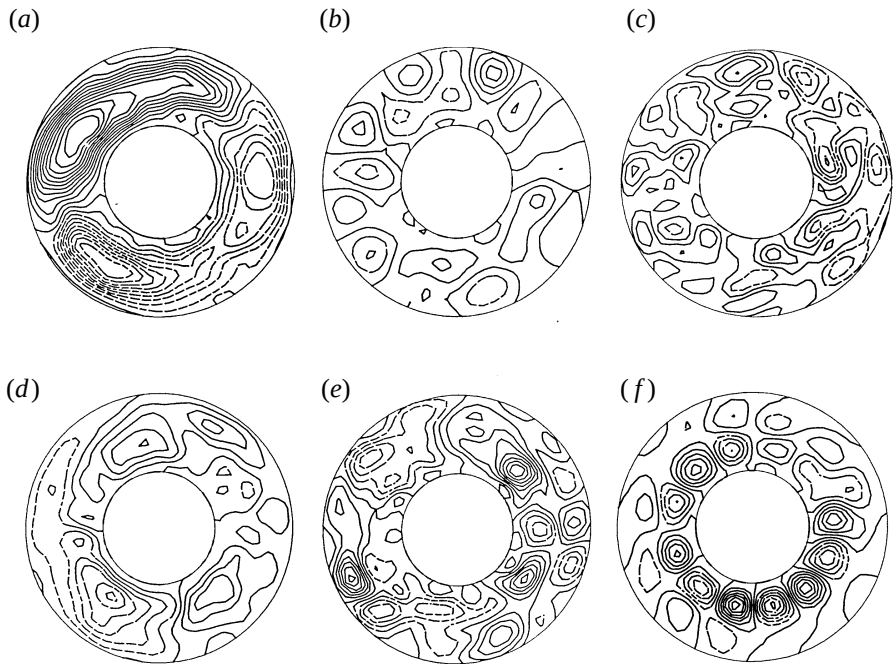

FIGURE 5. Eddy horizontal streamfunction maps at the upper (*a–c*) and lower (*d–f*) measurement levels for the −35° endwall configuration. Maps correspond to the $m = 1$ and two irregular flows seen in figure 2. The lower-level streamfunction map for the regular $m = 1$ mode has been 'phase corrected' so that it is in the same time frame as the upper-level map. Contour intervals are 2 mm^2 s^{-1}.

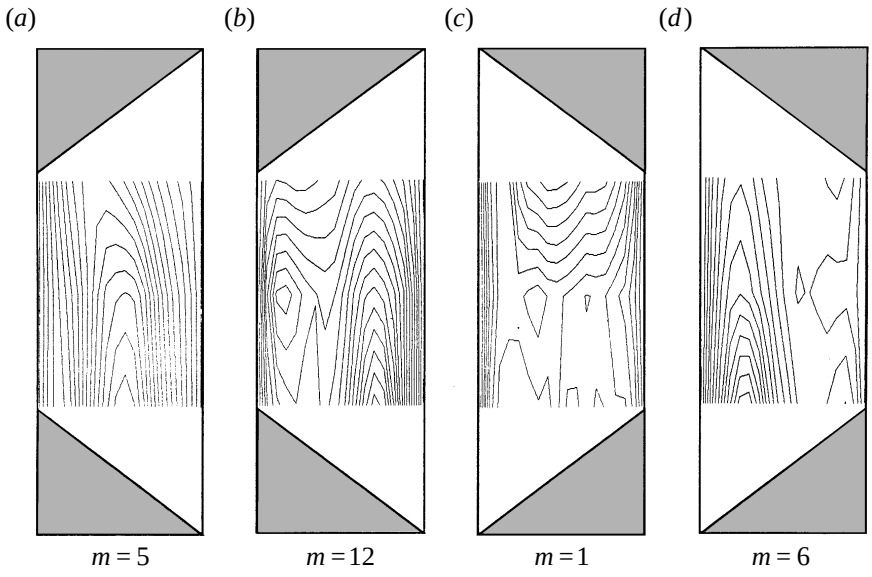

FIGURE 6. Contour maps in the meridional-height (r, z)-plane of the azimuthally averaged mean radial velocity amplitude $\left(|\, u^2 \,|\right)^{1/2}$ for the indicated dominant azimuthal wavenumbers in the +35° (*a, b*) and −35° (*c, d*) experiments. Maps shown correspond to the regular $m = 5$ (*a*), double eddy train (*b*), regular $m = 1$ (*c*) and high-Taylor-number irregular flows seen in figure 2. The contour intervals are 0.025 (c) and 0.05 mm s^{-1}.

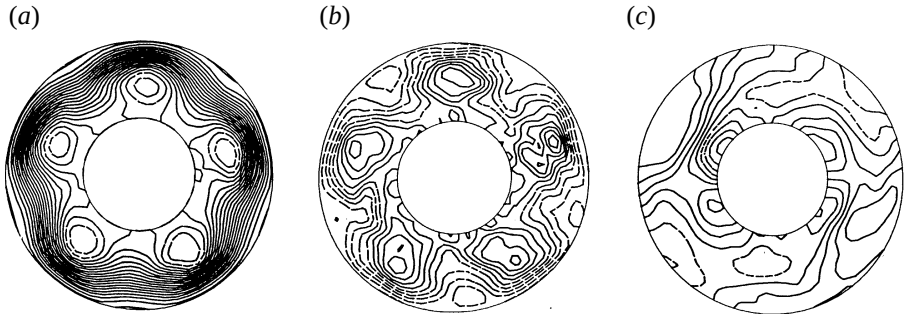

FIGURE 7. Total horizontal streamfunction (*a*) and total QG potential vorticity (*b*) maps obtained at mid-level for the $m = 5$ mode of figure 2. Also shown is the upper-level total velocity potential (*c*) map for the $m = 2$ mode of figure 2. Contour intervals are 5 mm^2 s^{-1} (*a*), 0.3 s^{-1} (*b*) and 1 mm^2 s^{-1} (*c*).

with $\partial D/\partial r < 0$ endwalls. This radial confinement appears to be related to the radial variation in the fluid depth, with the eddies being confined close to where the depth of the fluid is largest (see figure 6*b*, *d*).

The addition of oppositely sloping endwalls does not, however, radically alter the vortex character of the eddy features produced by internal heating and sidewall cooling. This is illustrated in figure 7 which shows maps of the total horizontal streamfunction (*a*) and QG potential vorticity (*b*) at the mid-level ($z/\overline{D} = 0.44$) for the $m = 5$ regular mode of figures 2 and 4. The closed 'pools' of potential vorticity indicate that fluid may be trapped for extended periods within these baroclinic eddies, as demonstrated by the dye-tracer experiments of RLH. In the regular wave regime of all but the $-35°$ experiments, the eddy features still appear to have an approximately equivalent-barotropic structure at their centre once the drift of the eddies between scans of each level is removed. Unlike the f-plane regular modes, however, their amplitude varies considerably with height, with the eddy features produced with $\partial D/\partial r < 0$ ($\partial D/\partial r > 0$) endwalls being stronger towards the top (bottom) boundary. As is argued later, this vertical trapping may be a consequence of the structure of the azimuthally averaged zonal mean flow generated by the two endwall configurations and its respective strength at each different level in the fluid.

Finally, there also appears to be a significant divergent component in these flows. This is illustrated in figure 7(*c*) where the upper-level horizontal velocity potential map for the $+35°$ $m = 2$ mode discussed above is displayed. This velocity potential map, which is derived following the method of Read (1990), effectively shows the magnitude of the divergent, and hence ageostrophic, component of the flow. It can be seen that the magnitude of the velocity potential represents between approximately 30% and 50% of its streamfunction field at this level. As discussed below, this large divergent component has implications for the numerical modelling of these internally heated flows, indicating as it does why neither linear nor QG theory will be able to reproduce the considerable asymmetry between the regular wave regimes generated in the steep $\partial D/\partial r > 0$ and $\partial D/\partial r < 0$ endwall experiments.

4.3. *Eddy phase velocities*

The radial variation in fluid depth introduces a considerable dispersive component to the flow, causing the eddy features to drift relative to the walls of the apparatus. In order to identify essentially nonlinear effects within the fluid, Mason (1975) compared the drift rates of the regular waves seen in his wall-heated system with theoretical

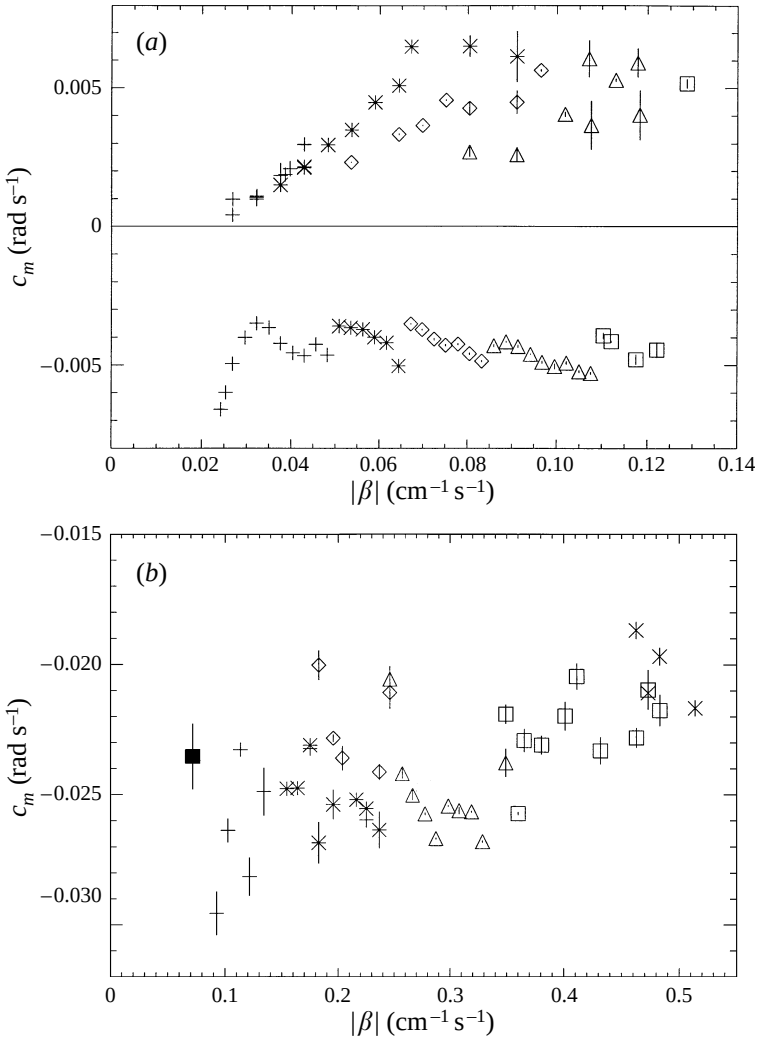

FIGURE 8. Measured angular phase velocity c_m versus barotropic β averaged over the three measurement levels of the experiment for $\pm 12^\circ$ (*a*) and $+35^\circ$ (*b*) regular flows. The azimuthal wavenumber of the flow is denoted as follows: $m = 2$ (closed square), $m = 3$ (plus), $m = 4$ (asterisk), $m = 5$ (diamond), $m = 6$ (triangle), $m = 7$ (open square) and $m = 8$ (cross).

drift rates for both barotropic Rossby waves and those obtained from the linear perturbation theory of Hide (1969). He found that the measured drift rates were between 40% and 80% of the theoretical values. Within the linear perturbation theory, the phase speeds of the waves are dependent on, amongst other factors, the ratio of the endwall slope to that of the isotherms. It is not practical with the present experimental setup to measure the internal temperature structure of the fluid, thus precluding detailed comparison with this theory. It is possible, however, to see how the phase speeds of the regular modes of the current experiment compare with those of barotropic Rossby waves, and this is undertaken below.

In both $+12^\circ$ and $+35^\circ$ experiments, the eddies were observed to drift in an 'easterly' or clockwise sense relative to the walls of the apparatus, while those of the -12° and -35° experiments drifted in a 'westerly' sense ahead of the rotation of the

system. The smaller-wavenumber eddies (especially the $m = 1$ mode of the -35° set) were seen to drift faster than the higher-wavenumber modes, which is in qualitative agreement with the barotropic Rossby wave dispersion relation

$$c_b = -\frac{\beta}{\left(2m/(b+a)\right)^2 + \left(\pi l/(b-a)\right)^2}, \tag{4.3}$$

which associates large phase speeds with smaller wavenumbers. Figure 8 shows the measured eddy phase velocity c_m averaged over the three levels of the experiment as a function of barotropic β for $\pm 12^\circ$ (*a*) and $+35^\circ$ (*b*) endwall configurations. The phase velocity of a mode is defined as ω_d/m, where the measured drift frequency ω_d is obtained from the Fourier components of the radial velocity fields fitted to the flow (cf. Hignett *et al*. 1985). In only the $+12^\circ$ experiment is there any apparent pattern in the phase velocities, which form small almost straight 'bands' for each different wavenumber. These bands do not intersect with the origin (as barotropic β tends to zero), however, as might be expected from the above dispersion relation. This pattern is less distinct in the $+35^\circ$ experiment where the magnitude of the phase velocity is fairly constant around $2\text{–}3 \times 10^{-2}$ rad s^{-1} for all wavenumbers. The phase velocities of the -35° $m = 1$ mode were more difficult to measure from the fitted Fourier components due to their small amplitude and vertically trapped nature.

Table 2 shows the ratio of the measured eddy phase velocity c_m to that of barotropic Rossby waves c_b (with unity indicating agreement between observation and the above dispersion relation), calculated for the observed azimuthal wavenumber m and first radial mode structure ($l = 1$). In all but the -12° experiments, the best agreement between the measured phase velocity and the above dispersion relation is obtained for the low azimuthal wavenumber flows. As the Taylor number (and hence azimuthal wavenumber) increases, however, the ratio c_m/c_b decreases to values close to approximately 0.35. One possible explanation for this may be that the effective 'β term' experienced by these flows is smaller than that given by the calculated barotropic β of equation (2.1). In addition, Mason (1975) notes that processes that would be expected to cause the waves to drift relative to the apparatus can be split up into those which produce a net zonal mean flow (such as the curvature of the apparatus, sloping geopotentials and variations of the physical properties of the fluid with temperature), and those which make the waves propagate relative to the zonal mean flow. In the f-plane experiments, it is primarily the former which causes the small drift in the eddies relative to the walls of the annulus (typically around $1\text{–}2 \times 10^{-3}$ rad s^{-1}), effectively Doppler-shifting each wave component by an equal amount. As the endwall slope becomes steeper, however, it appears that the latter effect becomes more significant in determining the phase speed of the eddies. Nevertheless, the values for c_m/c_b obtained in this study are remarkably close to those obtained by Mason.

4.4. *Zonal mean flow structure*

The change in sign of the laterally imposed temperature gradient, created by the internal heating and sidewall cooling, is expected to give rise to two opposing zonal jets in 'thermal wind balance' centred close to the top and bottom boundaries (Hide & Mason 1970; Read 1986*a*). In the f-plane experiment (RLH) the symmetry of the horizontal endwalls causes these zonal jets to be approximately anti-symmetric about mid-depth, while the zonally averaged horizontal temperature gradient changes sign across the lateral domain indicating the existence of a 'thermal equator' near mid-radius. The introduction of a radial depth gradient might be expected to alter

$+35^\circ$			$+12^\circ$			-12°		
$\tau \times 10^7$	m	c_m/c_b	$\tau \times 10^7$	m	c_m/c_b	$\tau \times 10^7$	m	c_m/c_b
0.13	2	0.81	0.20	3	0.75	0.46	3	0.15
1.11	5	0.63	1.75	5	0.31	1.87	5	0.33
7.39	8	0.46	4.39	7	0.36	5.59	7	0.35

TABLE 2. Comparison of the ratio of the observed phase velocity c_m to the theoretical phase velocity of barotropic Rossby waves c_b for a range of regular modes seen with $+35^\circ$ and $\pm 12^\circ$ endwall configurations. Unity indicates agreement between observation and the barotropic Rossby wave dispersion relation (4.3).

this background mean flow structure, perhaps through the blocking of the inverse energy cascade of the barotropic components of the flow (Rhines 1975, 1979). In the following section we shall therefore investigate whether the complex mean flow structure of this experiment is modified by the presence of a radial depth gradient, and if any increase in the observed number of zonal jets can be linked to the Rhines effect.

Figure 9 shows several examples of (r, z) cross-sections of the time-averaged zonal mean flow $\overline{v}$ in the axisymmetric (a, d), regular (b, e), and high Taylor number (c, f) flow regimes of both 35° endwall configurations. The zonal mean flow in the $+35^\circ$ experiments is dominated by a strong prograde jet which extends over the full range of the fluid depth measured, thus removing the approximate antisymmetry of $\overline{v}$ about mid-depth seen in the f-plane experiments. The axisymmetric flow is entirely prograde and has a strong barotropic component superimposed on the vertically sheared current, with the retrograde jet at the lower level being only just visible close to the inner cylinder. As Ω increases this prograde jet becomes radially confined close to the outer cylinder, with retrograde flow appearing towards the inner cylinder. While at the lower levels there are only the two opposing zonal jets expected from the background thermal forcing, at the upper level there is evidence for an increase in the radial wavenumber of the zonal mean flow, with three, and perhaps even four, zonal jets being observed. The prograde jet adjacent to the inner cylinder is initially localized close to the top boundary (b), but as Ω increases this jet extends deeper into the body of the fluid, so that at the highest Taylor numbers three distinct opposing zonal jets are seen above mid-level (c). A similar increase in the radial wavenumber of the zonal mean flow at the upper level is also seen in the $+12^\circ$ experiments, although the prograde jet centred close to the inner (outer) cylinder does not extend as close to mid-level (upper level) as in the steeper endwall set. Furthermore, these additional zonal jets are observed over a much smaller range of Taylor number space than in the steeper endwall arrangement.

This evolution of the zonal mean flow from a single prograde barotropic jet in the axisymmetric regime to multiple zonal jets in the double eddy train regime may be linked to the apparent migration of the thermal equator from the inner to the outer cylinder as Ω is increased. In fact, this process proceeds so far that a second thermal equator appears close to the inner cylinder in the double eddy train regime. Comparison of the total horizontal streamfunction map of figure 2(c) with figure 9(c) shows that each eddy train is centred on a different thermal equator, with the sense of circulation of the eddies given by the horizontal shear of the background flow. This is remarkably different from the f-plane experiment, in which only a single

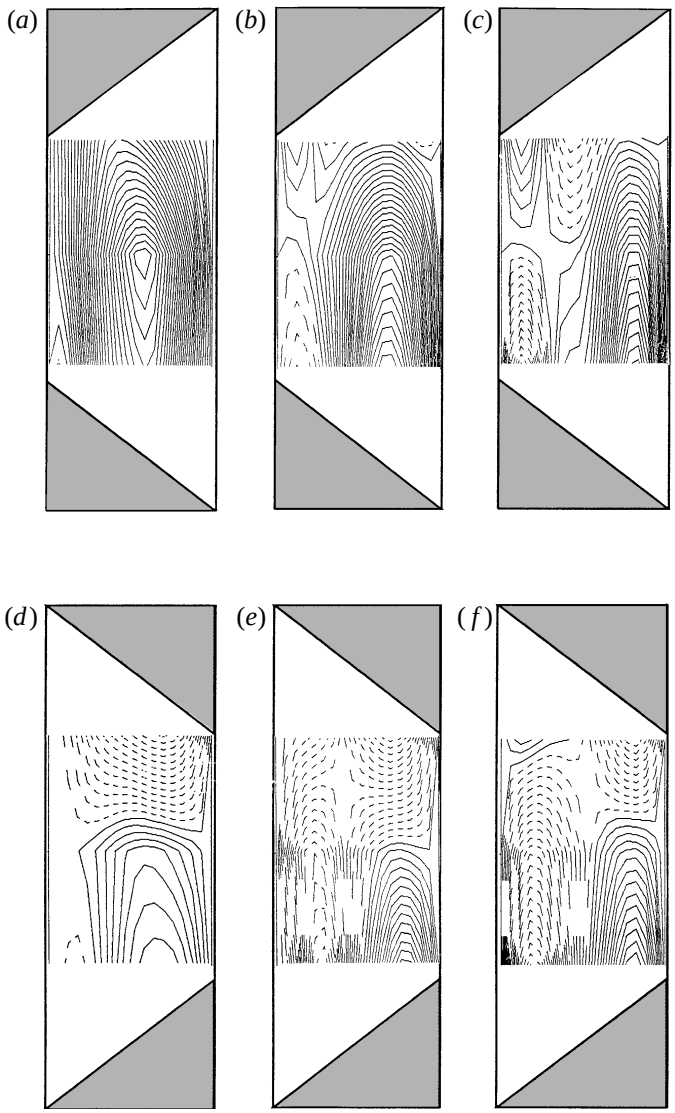

FIGURE 9. Contour maps in the meridional-height (r, z)-plane of the azimuthally-averaged zonal mean flow for $+35°$ (*a–c*) and $-35°$ (*d–f*) endwall configurations. Maps shown correspond to the following flow regimes: (*a*) axisymmetric ($S = 1.89$, $\tau = 6.99 \times 10^5$); (*b*) regular ($S = 0.152$, $\tau = 1.11 \times 10^7$); (*c*) double eddy train ($S = 0.013$, $\tau = 1.96 \times 10^8$); (*d*) axisymmetric ($S = 1.98$, $\tau = 7.03 \times 10^5$); (*e*) regular ($S = 0.233$, $\tau = 6.40 \times 10^6$); (*f*) irregular ($S = 0.015$, $\tau = 1.97 \times 10^8$). Positive contours indicate prograde flow. The contour interval is 0.15 mm s^{-1}.

thermal equator, centred close to the geometric centre of the channel, is observed at the highest Taylor numbers.

In contrast, the zonal mean flow in the $-35°$ experiments is dominated by the retrograde jets, which almost entirely fill the gap width above mid-depth. The prograde jet close to the outer cylinder is considerably weaker than in the $+35°$ arrangement, extending only up to mid-depth. The prograde jet at the upper level is only seen close to the inner cylinder at the highest Taylor numbers. No increase in the mean flow radial wavenumber (above the two expected from geostrophy) can be

detected in the mean flow cross-sections of either the -12° or -35° arrangements. Although the thermal equator is once again centred towards the outer cylinder at high Taylor numbers, no additional thermal equator forms closer to the inner cylinder as occurs in the $+35^\circ$ experiments.

It is therefore evident that the introduction of oppositely sloping endwalls causes the zonal mean flow to develop a significant barotropic component that is superimposed on the background vertically and horizontally sheared double jet structure generated by the non-monotonic thermal gradient of the experiment. This barotropic component is predominantly prograde (retrograde) in the $\partial D/\partial r > 0$ ($\partial D/\partial r < 0$) experiments, and is increasingly confined close to the outer (inner) cylinder where the fluid depth is greatest. Furthermore, this 'barotropization' of the flow becomes more pronounced as the amplitude of the top and bottom boundary slope is increased.

4.5. *Eddy kinetic energy spectra*

If the formation of the additional zonal jets seen at high Taylor numbers in the $\partial D/\partial r > 0$ endwall experiments results from the blocking of the inverse energy cascade of the barotropic eddy component of the flow due to the presence of the radial depth gradient, then the L_β scale is expected to dominate the flow and to be coincident with scale of maximum eddy kinetic energy. This can be determined by plotting the time-averaged eddy spectral energy density $E(\kappa)$ (§3.1) as a function of the dimensional total wavenumber κ, and investigating whether there is a peak, or change of gradient, in $E(\kappa)$ close to the $\kappa_\beta = \left(\beta/2v_{r.m.s.}\right)^{1/2}$ scale. To reflect the fact that the Rhines argument relates to the barotropic component of the flow, κ_β has been calculated from a zonal velocity scale obtained from the vertically averaged $m = 0$ components of the azimuthal Fourier series fitted to the zonal mean flow. This barotropic zonal velocity scale has the form

$$v_{r.m.s.} = \frac{1}{3}\left\{\int_a^b (\overline{v_1} + \overline{v_2} + \overline{v_3})^2 \,\mathrm{d}r \Big/ \int_a^b \mathrm{d}r\right\}^{1/2}, \tag{4.4}$$

where $\overline{v_1}$, $\overline{v_2}$ and $\overline{v_3}$ are the azimuthally averaged zonal velocity scales obtained at the upper, middle and lower measurement levels of the experiment. The barotropic β-term is given by (2.1).

Figure 10 shows plots of $E(\kappa)$ at upper and lower levels for the $+35^\circ$ double eddy train flow (a, b) and the -35° high Taylor number irregular flow (c, d) discussed above. In the former, there appears to be a clear correspondence between κ_β and the scale of maximum eddy kinetic energy κ_M, which indicates that this is the scale at which the eddy kinetic energy is being blocked. The similarity in the scale of κ_M at both the upper and lower levels is also reflected in the corresponding eddy streamfunction plots of figures 4(c) and 4(f) where there appears to be little difference in the size of the eddies at the two levels. The κ_β scale is also found to be close to κ_M at high Taylor numbers in both 12° endwall arrangements.

A different situation is seen in the -35° example, where the eddy kinetic energy has clearly penetrated κ_β at both levels. This is reminiscent of the work of Shepherd (1987), who found that the disturbance field of barotropic β-plane turbulence could penetrate the Rhines radius in the presence of a strong zonal shear flow. He also observed that, at the largest scales, the eddies developed meridional rather than the zonal anisotropy suggested by Rhines. It is not obvious from the eddy streamfunction plots (figure 5c, f) whether these high-Taylor-number eddies are indeed developing meridional rather than zonal anisotropy, but they do appear to be larger than those

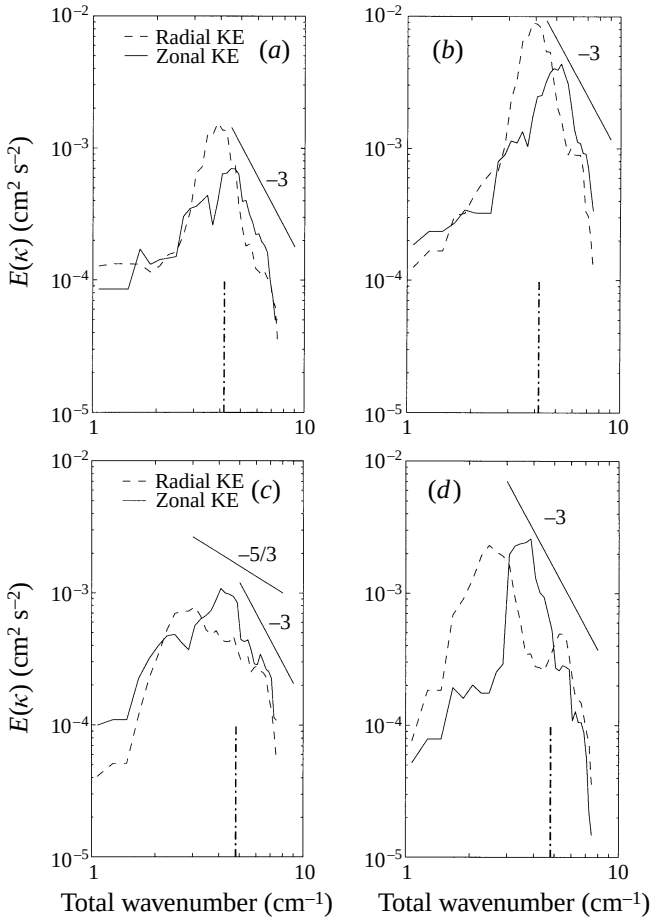

FIGURE 10. Eddy spectral energy density $E(\kappa)$ versus total dimensional wavenumber κ (multiplied by 2 for plotting purposes) at upper (a, c) and lower (b, d) measurement levels for the $+35°$ double eddy train flow (a, b) and $-35°$ high Taylor number irregular flow shown in figure 2. The position of the κ_β scale is indicated by the vertical dot-dashed line.

observed in the double eddy train flows at approximately the same Burger number (figure 4c, f).

A second important length scale in this problem is the Rossby deformation radius L_r, which is the scale where the barotropic component of the flow is 'stirred' by baroclinic instability. For the two high-Taylor-number flows discussed here, L_r (obtained from their respective Burger numbers) has approximate values of 0.7 cm and 0.75 cm. In the total wavenumber space of figure 11, these values correspond to $\kappa = 9.0$ and 8.4 cm^{-1}, and are close to the smallest scales that can be resolved in the current system. It is therefore not clear whether L_r does play a direct role in determining the scale of these jets, or if indeed, as required by the Rhines argument, there is the large inertial range separating L_r and L_β for the inverse energy cascade.

In figures 10(a), 10(b) and 10(d) there appears to be little evidence for the existence of an inertial range with a slope close to $\kappa^{-5/3}$ which might correspond to an inverse energy cascade. At higher wavenumbers than κ_β, the spectral slope is, in fact, much

steeper than $\kappa^{-5/3}$, being greater than or approximately equal to the κ^{-3} which characterizes an enstrophy cascade in the classical theory of geostrophic turbulence (Charney 1971). There does, however, seem to be a range in the radial component of $E(\kappa)$ at the upper level for the -35° example (figure 10*c*) which has a slope close to $\kappa^{-5/3}$. Nevertheless, this range clearly extends beyond κ_β indicating that the energy component is not blocked by the Rhines effect. Such a situation is not only interesting for the reasons outlined above, but also because this is the level at which the single isolated vertically trapped -35° $m = 1$ mode was observed. Figure 10(*c*) may thus be further reflecting the observation that with a large negative radial depth gradient the eddy kinetic energy is apparently trapped close to the largest scales in the flow, and this trapping may be a consequence of an inverse energy cascade to the larger scales of motion which is not blocked by the Rhines effect.

4.6. *Multiple zonal jets and the Rhines scale*

Given that the eddy kinetic energy appears to be blocked close to the κ_β scale at high Taylor numbers in all but the -35° experiments, it is of interest to determine whether the Rhines scale can be used to predict quantitatively the number of zonal jets seen in each endwall configuration. This is investigated in figure 11, which shows values for $N_j = (b-a)/L_\beta$, effectively the number of zonal jets expected from the barotropic theory, against Taylor number for both 35° endwall configurations. The Rhines scale has been calculated using the barotropic zonal velocity scale $v_{r.m.s.}$ described above. To reduce random errors in $v_{r.m.s}$ (and hence N_j) five sets of scans were analysed for each measurement of $v_{r.m.s.}$ and the results combined to yield a mean and standard deviation. Formal uncertainties in N_j are in the range 1–10% (typically 5%).

In the $+35^\circ$ experiments N_j reaches values close to 4 at the highest Taylor numbers, which is in good quantitative agreement with the three to four zonal jets actually observed at the upper/middle level with this endwall arrangement. This correspondence between N_j and the radial wavenumber of the mean flow is not, however, reproduced at either the lower level of the $+35^\circ$ set, or at any of the three levels in the -35° experiments, where only the two strong zonal jets generated by the thermal forcing are evident in the (r, z) profiles of $\bar{v}$ (figure 9). A similar situation is seen in the 12° endwall experiments, with N_j reaching values of approximately 3 at the highest Taylor numbers, which is in reasonable agreement with the number of zonal jets detected at the upper level of the $+12^\circ$ experiments. At lower levels, and in the -12° set, N_j once again overestimates the number of zonal jets observed in the flow, although not to the same extent as in the 35° endwall experiments. Thus, it appears that the Rhines scale can approximately predict the radial wavenumber of the mean flow in the $\partial D/\partial r > 0$ endwall experiments, but only in regions where the background thermally forced zonal jets are weak.

In summary, while there is evidence for the existence of multiple zonal jets in these baroclinic $\partial D/\partial r > 0$ endwall experiments, it still remains uncertain what role, if any, the barotropic arguments of §1 have in their formation. As noted previously, the introduction of steep oppositely sloping boundaries causes the zonal mean flow to develop a significant barotropic component to which the Rhines argument should apply. Consideration of figure 11 shows that at the highest Taylor numbers there is not a great difference in the values of N_j for the two endwall configurations (4.2 to 4.7 for 35° experiments and 3.1 to 3.2 for the 12° experiments (not shown)). This suggests that in terms of the barotropic theory at least, there should only be a small difference in the number of zonal jets seen in each experiment, and it is just the presence of the strong thermally forced zonal jets which effectively mask the relatively weaker

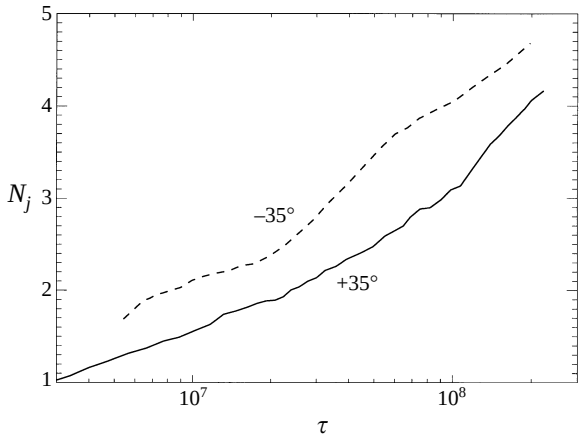

FIGURE 11. The number of zonal jets expected from the barotropic theory N_j versus Taylor number for the $\pm 35^\circ$ experiments.

zonal jets produced by barotropic β-plane turbulence. This appears to be the case in the $\partial D/\partial r > 0$ endwall experiments, since figure 10 shows that the eddy kinetic energy is blocked close to the Rhines scale at both the upper and lower levels at high Taylor number in the $+35^\circ$ experiments. However, while the values of N_j are in good agreement with the number of zonal jets seen at upper levels in the $\partial D/\partial r > 0$ endwall experiments, it does not explain why the eddy kinetic energy appears to have penetrated the Rhines scale at the highest Taylor numbers in the -35° experiments. If we appeal to the ideas of Shepherd (1987) then the eddy kinetic energy should also penetrate the Rhines scale at the two lower levels in the $+35^\circ$ experiments, where the mean flow is as large as it is in the -35° set. Clearly, this is highlighting a difference in the effect the two opposite senses of boundary slope have on the flow structure when the endwall slope is large. This disparity cannot be explained purely in terms of simple barotropic ideas, or indeed QG theory, but may find expression in the primitive equations of the system.

5. Discussion

In this study we have extended the work of Read & Hide (1983, 1984) and RLH by investigating how a radial depth gradient modifies the flow regimes seen in a fluid system heated internally and cooled at the side boundaries. Stable, regular eddy features are seen with both $\partial D/\partial r > 0$ (fluid depth increasing with radius) and $\partial D/\partial r < 0$ (fluid depth decreasing with radius) boundary configurations, even those with the largest values of endwall slope. These regular modes still comprise a series of closed compact oval anti-cyclonic eddies (at the upper level), as in the f-plane experiment, but which now have a large net drift relative to the walls of the apparatus. Values for the drift rates of these regular modes are between 30% and 80% of those given by the barotropic Rossby wave dispersion relation (4.3). A role for nonlinear interactions in suppressing the dispersion of the constituent wave components of these eddy structures is suggested by the closed contours of QG potential vorticity, which also indicates that fluid may be trapped for extended periods within these baroclinic 'vortices' (Lewis 1992; Read 1993; RLH).

Within the linear perturbation theory of Hide (1969), there should be no quanti-

tative difference between the regular wave regimes produced by a positive/negative radial depth gradient. This is essentially what is observed when the endwall slope is small, as the regular wave regime of the $\pm 12^\circ$ experiments are seen to consist of regular modes $m = 3$ to 7. At larger values of endwall slope this symmetry is lost, however, with regular modes $m = 2$ to 8 being observed in the $+35^\circ$ experiments, but only the single $m = 1$ mode in the -35° set. Such differences clearly cannot be explained purely in terms of linear perturbation theory, nor even QG theory, due to the presence of the significant divergent component of these flows.

While the introduction of a radial depth gradient does not preclude the existence of stable, regular eddy modes, oppositely sloping endwalls are found to modify both the horizontal and vertical structure of the eddy features seen in this experiment. As Ω increases, the radial scale of the eddy features is seen to decrease to values less than that of the gap width. This is similar to the findings of Mason (1975) who also observed a reduction in the radial scale of baroclinic waves at high rotation rates and steep endwall slopes in his wall-heated system. The reduction in the radial extent of these internally heated eddy features is most pronounced in the $\partial D/\partial r > 0$ endwall experiments, where two independent trains of eddies are seen to form in the lateral domain at the highest Taylor numbers. This double eddy train is most clearly seen at the upper level of the experiment, although there appears to be very little qualitative difference in the structure of the eddy circulations at the different levels, suggesting that the strong mean flow existing at the lower levels may be masking these weaker features. Conversely, although the radial extent of the eddies is less than half that of the gap width at the highest Taylor numbers in the -35° experiments, a double eddy train is not evident at any of the three levels. Once again this may be partly due to the relative strength of the mean flow at each level, but also to the structure of the eddies seen in the -35° experiments, which appear to be both stronger and adopt a larger radial scale than their $+35^\circ$ counterparts.

A further effect of steep oppositely sloping boundaries, not noted by Mason, is the reduction in the vertical as well as the radial scale of the eddies. The regular modes of these internally heated experiments appear to be vertically trapped close to the lower (upper) level in the $\partial D/\partial r > 0$ ($\partial D/\partial r < 0$) endwall experiments. Careful examination of the (r, z) profiles of the azimuthally-averaged zonal mean flow show that the magnitude of $\overline{v}$ is also largest towards the lower (upper) level in the regular wave regime of the $+35^\circ$ (-35°) experiments. Global energy budgets for examples of internally heated regular f-plane eddy flows show that their kinetic energy is maintained against viscous and thermal diffusion predominantly by baroclinic conversions from the potential energy of the mean flow, but also partly through barotropic conversions arising from the strong lateral shear of the zonal mean flow (Hide *et al.* 1994; RLH). There is no reason to suppose that introducing oppositely sloping endwalls will radically alter these basic energetics, so it is perhaps to be expected that the eddy features will also be strongest in the regions where $\overline{v}$ is greatest. This is most clearly demonstrated in figures 6 and 9 where the correspondence between the vertical structure of the zonal mean flow (9*e*, 9*f*) and the apparent vertical trapping of the -35° regular $m = 1$ (6*c*) and irregular $m = 6$ (6*d*) modes close to the top and bottom boundaries is striking. These figures further reflect the experimental observation that while the regular $m = 1$ mode of the -35° experiments was localized close to the upper level, the high-Taylor-number irregular flows were strongest at the lower level. It is interesting to note that vertical trapping is also a feature of the Charney model of baroclinic instability, and Green's (1960) β-plane extension to the Eady model. Green found that the minimum in the perturbation pressure amplitude

(close to the steering level where $U \sim c$) moved from mid-depth when $\beta = 0$ (the Eady problem) to near the bottom boundary when $\beta > 0$.

In the f-plane experiment the distribution of internal heating and sidewall cooling gives rise to a mean flow structure which consists of two opposing zonal jets at each measurement level. The inclusion of oppositely sloping endwalls has been seen to alter radically this situation, with the formation of between one and two additional zonal jets at the upper level in both the $+12^\circ$ and $+35^\circ$ experimental sets. These additional zonal jets are highly localized in the vertical and only penetrate to mid-depth at the largest Taylor numbers. The radial scale of these multiple zonal jets is in reasonable quantitative agreement with the Rhines scale L_β. At lower levels, the mean flow is very much stronger and retains the double jet structure expected from the thermal forcing. This increase in the number of zonal jets in regions where the background mean flow is weak, but which are not seen when the thermally forced mean flow is stronger, has parallels with the work of Shepherd (1987) who investigated how forced homogeneous barotropic β-plane turbulence was altered in the presence of a large-scale barotropically stable zonal flow. He found that as the flow evolved, the disturbance enstrophy was transferred along lines of constant zonal wavenumber through shear-induced nonlinear interactions with the mean flow, with the result that the disturbance field penetrated the Rhines scale and developed meridional rather than the expected zonal anisotropy. It is not possible with the limited spectral resolution of the data in the present experiment to develop the sophisticated spectral diagnostics required to verify whether these spectral transfers are indeed occurring. In the -35° experiments, however, there is evidence that the eddy kinetic energy has penetrated beyond the Rhines scale in the presence of the strong mean flow at the largest Taylor numbers. This is not reproduced in the $+35^\circ$ experiments (or the 12° experiments) where, even at the lower levels in the presence of strong thermally forced jets, the maximum in the eddy kinetic energy is approximately coincident with the Rhines scale.

It is thus evident that while we have observed evidence for the formation of multiple zonal jets in a baroclinic fluid, the identification of the processes which give rise to them is complicated by the complex structure of the background mean flow generated by the thermal forcing of this experiment. The structure of this background mean flow also makes direct comparison with numerical models used to investigate baroclinic turbulence (e.g. Panetta 1993) difficult. Therefore, a system with a simpler mean flow structure closer to that of the numerical models would be desirable to investigate further this important problem. Such a laboratory model is provided by the modification of the present system through the removal of the inner cylinder and its replacement by a thin wire, thereby simulating a polar β-plane (cf. Hide & Mason 1970). Since heat can only be extracted from the outer cylinder in this new experiment, the mean flow is expected to consist of a single jet (retrograde at the upper level, prograde at the lower) at each level. Work on this new open cylinder experiment is currently being undertaken and will be reported elsewhere.

However, the present experiment does, nevertheless, provide an important message for further numerical studies of rotating fluid systems. Within the simple linear instability theory and the fully nonlinear QG theory, the sign of β may be changed with little effect on the resulting flow structure. These experiments clearly demonstrate that this is not the case when the magnitude of the endwall slope becomes large, as endwalls which create a large positive radial depth gradient produce dramatically different flows to those seen with a large negative radial depth gradient. These differences cannot be due purely to nonlinear effects, but must in part be caused by

deviations from quasi-geostrophy in the interior of the fluid and at the boundaries. Therefore, while there may be a qualitative similarity between the f-plane steady wave features produced in QG models and those found in full Navier–Stokes simulations (Read 1985; Lewis 1992), QG theory will never be able to represent all aspects of these oppositely sloping boundary laboratory flows, since it is not able to account for ageostrophic advection by the significant divergent component of these flows.

It is a pleasure to thank Dr Steve Lewis for many useful discussions during the course of this work. The help received from Mr Mike Buckler in setting up the apparatus is also greatly appreciated. Funding for M.E.B. was provided by the UK Meteorological Office.

REFERENCES

Batchelor, G. K. 1967 *An Introduction to Fluid Dynamics*. Cambridge University Press.

Bell, M. J. 1984 The least squares method of Fourier analysing two-dimensional velocity data produced by the video velocity acquisition system. *Met. Off. Internal Rep.* **21** IR/84 (6). (Available from: Meteorological Office Library, London Road, Bracknell, Berkshire, RG12 2SZ, UK.)

Bell, M. J. & Jackson, W. D. N. 1985 Further analysis of methods for fitting fields to two-dimensional velocity data. *Met. Off. Internal Rep.* **21** IR/85 (1).

Busse, F. H. 1976 A simple model of convection in the Jovian atmosphere. *Icarus* **29**, 255–260.

Buzyna, G., Pfeffer, R. L. & Kung, R. 1984 Transitions to geostrophic turbulence in rotating differentially heated annulus of fluid. *J. Fluid Mech.* **145**, 377–403.

Charney, J. G. 1971 Geostrophic turbulence. *J. Atmos. Sci.* **28**, 1087–1095.

Green, J. S. A. 1960 A problem in baroclinic instability. *Q. J. R. Met. Soc.* **86**, 237–251.

Hide, R. 1969 Some experiments on free thermal convection in a rotating fluid subjected to a horizontal temperature gradient. In *The Global Circulation of the Atmosphere*. R. Met. Soc.

Hide, R., Lewis, S. R. & Read, P. L. 1994 Sloping convection: A paradigm for large-scale waves and eddies in planetary atmospheres? *Chaos* **4**(2), 135–162.

Hide, R. & Mason, P. J. 1970 Baroclinic waves in a rotating fluid subject to internal heating. *Phil. Trans. R. Soc. Lond.* A **268**, 201–232.

Hide, R. & Mason, P. J. 1975 Sloping convection in a rotating fluid. *Adv. Phys.* **24**, 47–99.

Hignett, P., White, A. A., Carter, R. D., Jackson, W. D. N. & Small, R. M. 1985 A comparison of laboratory measurements and numerical simulations of baroclinic wave flows in a rotating cylindrical annulus. *Q. J. R. Met. Soc.* **111**, 131–154.

Ingersoll, A. P. & Miller, R. L. 1986 Motions in the interiors and atmospheres of Jupiter and Saturn. 2: Barotropic instabilities and normal modes of an adiabatic planet. *Icarus* **65**, 370–382.

Ingersoll, A. P. & Pollard, D. 1982 Motions in the interiors and atmospheres of Jupiter and Saturn. *Icarus* **52**, 62–80.

Jackson, W. D. N. & Hignett, P. 1984 A system for the real-time measurement of two-dimensional velocity fields. *Met. Off. Internal Rep.* **21** IR/84 (1).

Kuo, H. L. 1950 The motion of atmospheric vortices and the general circulation. *J. Met.* **7**, 247–258.

Kuo, H. L. 1951 Vorticity transfer as related to the development of the general circulation. *J. Met.* **8**, 307–315.

Kuo, H. L. 1953 On the production of mean zonal currents in the atmosphere by large disturbances. *Tellus* **5**, 344–362.

Lewis, S. 1992 A quasi-geostrophic numerical model of a rotating internally heated fluid. *Geophys. Astrophys. Fluid Dyn.* **65**, 31–55.

Mason, P. J. 1975 Baroclinic waves in a container with sloping endwalls. *Phil. Trans. Roy. Soc.* A **278**, 397–445.

Panetta, R. L. 1993 Zonal jets in wide baroclinically unstable regions: persistence and scale selection. *J. Atmos. Sci.* **50**, 2073–2106.

Quon, C. 1977 Axisymmetric states of an internally heated rotating annulus. *Tellus* **29**, 83–96.

Read, P. L. 1985 Finite-amplitude, neutral baroclinic eddies and mean flows in an internally heated rotating fluid: 1. Numerical simulations and quasi-geostrophic 'free modes'. *Dyn. Atmos. Oceans* **9**, 135–207.

Read, P. L. 1986*a* Stable, baroclinic eddies on Jupiter and Saturn: a laboratory analogue and some observational tests. *Icarus* **65**, 304–334.

Read, P. L. 1986*b* Regimes of axisymmetric flow in an internally heated rotating fluid. *J. Fluid Mech.* **168**, 255–289.

Read, P. L. 1990 Determination of stream functions and velocity potentials using analysed velocity fields from VVAS data. *Met. Off. Internal Rep.* **21** IR/89 (1).

Read, P. L. 1993 Coherent baroclinic waves in a rotating, stably-stratified fluid and transitions to disorder flow. In *Waves and Turbulence in Stably Stratified Flows* (ed. S. D. Mobbs, J. C. King). Oxford University Press.

Read, P. L. & Hide, R. 1983 Long lived eddies in the laboratory and in the atmospheres of Jupiter and Saturn. *Nature* **302**, 126–129.

Read, P. L. & Hide, R. 1984 An isolated baroclinic eddy as a laboratory analogue of the Great Red Spot on Jupiter. *Nature* **308**, 45–48.

Read, P. L., Lewis, S. & Hide, R. 1997 Laboratory and numerical studies of baroclinic waves in an internally heated, rotating fluid annulus. A case of wave/vortex duality? *J. Fluid Mech.* **337**, 155–191 (referred to herein as RLH).

Rhines, P. 1975 Waves and turbulence on a β-plane. *J. Fluid Mech.* **69**, 417–443.

Rhines, P. 1979 Geostrophic turbulence. *Ann. Rev. Fluid Mech.* **11**, 401–441.

Shepherd, T. G. 1987 Rossby waves and two-dimensional turbulence in large-scale zonal jet. *J. Fluid Mech.* **183**, 467–509.

Tamaki, S. & Ukaji, K. 1986 Stationary baroclinic eddies produced in a rotating fluid annulus. *J. Met. Soc. Japan* **64**, 681–691.

Ukaji, K. 1979 Thermal and dynamic structures of convective motions in a rotating fluid annulus subject to internal heating. *J. Met. Soc. Japan* **57**, 532–547.

Veronis, G. 1963 On the approximation involved in transforming the equations of motion from a spherical surface onto a β-plane. *J. Mar. Res.* **21**, 110–124.